Spin Hall effect from hybridized 3*d*-4*p* orbitals

Yong-Chang Lau,[1,2,*] Hwachol Lee,[2] Guanxiong Qu,[1,2] Kohji Nakamura,[3] and Masamitsu Hayashi[1,2,†]
[1]*Department of Physics, The University of Tokyo, Bunkyo, Tokyo 113-0033, Japan*
[2]*National Institute for Materials Science, Tsukuba 305-0047, Japan*
[3]*Department of Physics Engineering, Mie University, Tsu, Mie 514-8507, Japan*

(Received 12 April 2018; revised manuscript received 4 January 2019; published 12 February 2019)

We show that a paramagnetic CoGa compound possesses large enough spin Hall angle to allow robust spin-orbit torque switching of perpendicularly magnetized ferrimagnetic MnGa films in CoGa/MnGa/oxide heterostructures. The spin Hall efficiency estimated via spin Hall magnetoresistance and harmonic Hall measurements is $+0.05 \pm 0.01$, which is surprisingly large for a system that does not contain any heavy metal element. First-principles calculations corroborate our experimental observations and suggest that the hybridized Co 3*d*–Ga 4*p* orbitals are responsible for the intrinsic spin Hall effect. Our results suggest that efficient spin current generation can be realized in intermetallics by alloying a transition metal with a *p*-orbital element and by Fermi-level tuning.

DOI: 10.1103/PhysRevB.99.064410

I. INTRODUCTION

Electrical manipulation of magnetization by spin-orbit torque (SOT) [1–9] has shown promise for realizing reliable magnetic memories and oscillators. Recent experiments have demonstrated charge-spin conversion efficiency that exceeds ~0.1 in 5*d* transition metals [2,10–13] and alloys formed by mixing among transition metals [6,7,14–17] or among *p*-block elements [3,18]. Meanwhile, the spin Hall effect (SHE) in binary systems consisting of a transition-metal element and a *p*-block element has only been experimentally explored for limited materials, such as in Cu-Bi alloys in the diluted limit [19] or in the case of oxygen incorporation in tungsten [20].

Here, combining experiments and first-principles calculations, we reveal spin current generation via SHE in a *d*-*p* binary system: the paramagnetic β-CoGa compound. The spin Hall efficiency of CoGa that contains no heavy element with strong spin-orbit coupling (SOC) is determined to be $+0.05 \pm 0.01$, surprisingly large compared to other 3*d* metals or alloys that have been reported so far [21,22]. Using CoGa as a seed layer [23,24], we experimentally demonstrate magnetization switching of a Mn-based ferrimagnetic tetragonal Heusler compound [25] (MnGa), a material system that can be applied to ultrafast spintronic applications owing to its high perpendicular magnetic anisotropy (PMA) [23,26], low Gilbert damping [27], high spin polarization [28], and large tunneling magnetoresistance (MR) [29]. The excellent agreement between the experimental spin Hall conductivity (SHC) of $143 \pm 30\,(\hbar/e)\,\Omega^{-1}\,\mathrm{cm}^{-1}$ and the calculated SHC of $140\,(\hbar/e)\,\Omega^{-1}\,\mathrm{cm}^{-1}$ suggests the observed SHC is mainly of intrinsic origin ($\hbar$ and e are the reduced Planck constant and the elementary charge, respectively). We further show that the nearly degenerate *d*-*p* hybridized bands near the Fermi level and the SOC are the two necessary conditions for obtaining appreciable SHC in CoGa.

II. EXPERIMENTAL RESULTS

A. Structural and magnetic properties

Equiatomic β-$Co_{50}Ga_{50}$ crystallizes in CsCl-type *B*2 structure (space group 221), as illustrated in Fig. 1(b), with Co and Ga occupying equivalent 1*a* (0, 0, 0) and 1*b* (0.5, 0.5, 0.5) sublattices, respectively. Off-stoichiometric Co(Ga)-rich compounds may retain the *B*2 structure by forming Co antisites (vacancies) in lieu of Ga (Co) [30]. Figure 1(a) defines the coordinate system and illustrates our typical stacks, which consist of MgO(001) substrate/$Co_{53}Ga_{47}$(CoGa)(*t*)/FM/$(Mg_2Al)O_y$(MAO)(2)/Ta(1) (in nanometers). See Secs. 1 and 2 of the Appendix for the details of sample preparation and characterization. FM denotes either a 2-nm-thick ferrimagnetic $Mn_{1.44}Ga$ (MnGa) with PMA or a 1-nm-thick in-plane magnetized ferromagnetic $Co_{20}Fe_{60}B_{20}$ (CoFeB) layer. The symmetrical θ-2θ x-ray-diffraction spectrum of a CoGa(5)/MnGa(10) heterostructure is plotted in Fig. 1(c). The appearance of a CoGa(001) superlattice peak confirms the *B*2 ordering. Detailed peak intensity analysis suggests the simultaneous presence of ~10% Co antisites and vacancies. The pole figure in Fig. 1(d) reveals the in-plane epitaxial relationship of the structure: MgO[110]//CoGa[100]//MnGa[100], with CoGa and MnGa making a 45° in-plane rotation with respect to the MgO lattice. The magnetic hysteresis loops measured using superconducting quantum interference device (SQUID) in vibrating-sample magnetometry mode of a CoGa(5)/MnGa(2) heterostructure is shown in Fig. 1(e). We find saturation magnetization M_s of ~400 emu/cm^3 and anisotropy field H_k of ~20 kOe, corresponding to an effective uniaxial anisotropy $K_{\mathrm{eff}} \approx M_s H_k/2 \sim 4 \times 10^6 \mathrm{erg/cm}^3$.

B. Current-induced SOT switching

The Hall resistance R_{xy} as a function of the out-of-plane field (H_z) for a Hall bar device patterned from the CoGa(5)/MnGa(2) heterostructure is shown in Fig. 1(f). The

*yongchang.lau@qspin.phys.s.u-tokyo.ac.jp
†hayashi@phys.s.u-tokyo.ac.jp

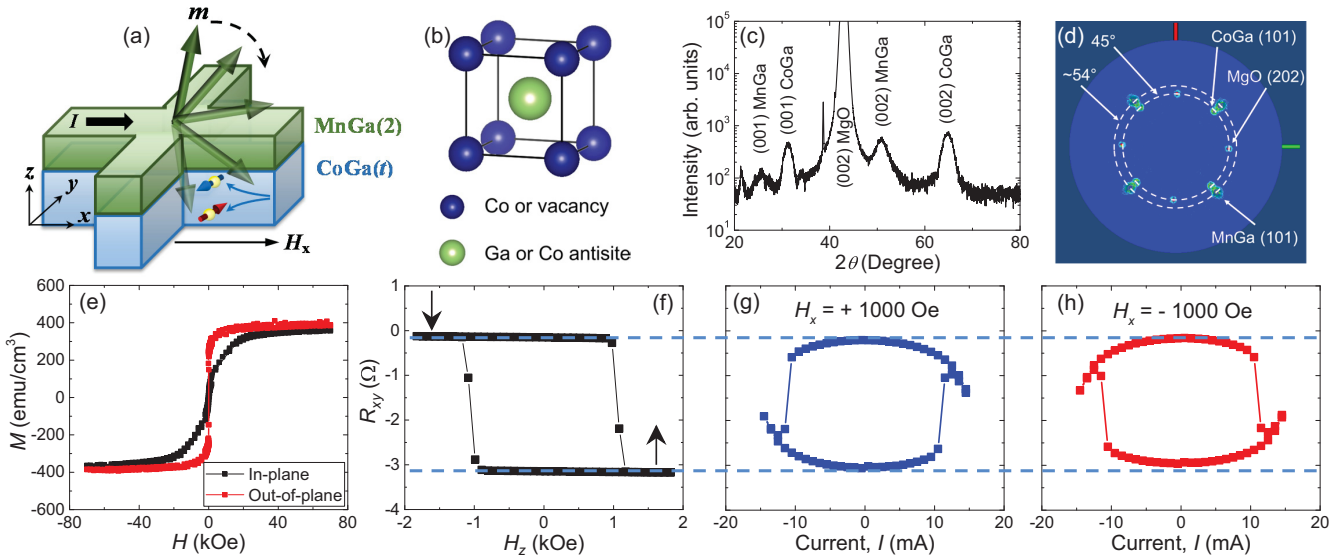

FIG. 1. (a) Schematic of the CoGa/FM bilayer with the definition of the coordinate system $(\boldsymbol{x}, \boldsymbol{y}, \boldsymbol{z})$. (b) Illustration of the $B2$ β-CoGa crystal structure. (c) θ-2θ x-ray-diffraction spectrum of a CoGa(5)/$Mn_{1.44}$Ga(10) bilayer deposited on a MgO(001) substrate. (d) Pole figure of the same stack, revealing the in-plane epitaxial relationship. (e) In-plane and perpendicular M-H loops of a CoGa(5)/$Mn_{1.44}$Ga(2) heterostructure. (f) Typical R_{xy}-H_z loop of a Hall bar device, confirming the strong PMA of MnGa. (g), (h) Current-induced SOT switching of the MnGa magnetization, monitored via R_{xy}, with an applied $\boldsymbol{x}$ field of ± 1 kOe. The two blue horizontal dashed lines indicate that practically all MnGa moments are reversed by the current.

square R_{xy}-H_z loop confirms the strong PMA of the magnetic layer with a coercive field $H_c \sim 1.2$ kOe. SOT-induced switching of MnGa is demonstrated by sweeping the current I along x while monitoring the z component of the magnetization via R_{xy}. R_{xy}-I loops, measured with a bias field $H_x = \pm 1$ kOe, are plotted in Figs. 1(g) and 1(h). Magnetization along $-z(+z)$ is preferred when the current flow and H_x are parallel (antiparallel), which suggests that the spin Hall angle of CoGa is positive (same sign with that of Pt [9]). Thus a charge current flowing along $+x$ generates a spin accumulation $(\boldsymbol{\sigma})$ polarized along $-y$ at the top interface of CoGa via the SHE. Using $\rho_{\mathrm{CoGa}} = 175\,\mu\Omega\,\mathrm{cm}$ and $\rho_{\mathrm{MnGa}} = 196\,\mu\Omega\,\mathrm{cm}$, obtained from the CoGa thickness dependence of the sheet conductance, the switching current $I_{\mathrm{sw}} \sim 11$ mA corresponds to a current density $J_{\mathrm{sw}} \sim 1.6 \times 10^7\,\mathrm{A/cm^2}$ in the CoGa layer.

C. Spin Hall magnetoresistance

The efficiency ξ_{SL} of the Slonczewski-like spin Hall torque acting on the adjacent magnetization $\boldsymbol{m}$ is linked to the intrinsic spin Hall angle θ by $\xi_{\mathrm{SL}} = T \cdot \theta$, where T $(\leqslant 1)$ describes the interfacial spin transparency [31]. From here on we focus on quantifying ξ_{SL} and its fieldlike counterpart ξ_{FL} of CoGa/MnGa and CoGa/CoFeB heterostructures to obtain the lower bounds of θ_{CoGa}. First we discuss ξ_{SL} obtained from magnetoresistance measurements. The longitudinal resistance (R_{xx}) of a heavy metal/ferromagnetic metal bilayer can be modulated by the transmission and reflection of SHE-induced spins at the interface due to the collective action of the SHE and the inverse SHE. Owing to this effect, now commonly referred to as the spin Hall magnetoresistance (SMR), R_{xx} shows a distinct difference when $\boldsymbol{m}$ is directed parallel or perpendicular to $\boldsymbol{\sigma}$ [32–34].

Figures 2(a) and 2(b) show the MR ratio—$\Delta R_{xx}(H_i)/R^i_{xx,0}$ with $i = x, y, z$—of CoGa(5)/$Mn_{1.44}$Ga(2) and CoGa(5)/CoFeB(1) heterostructures with magnetic field applied along three orthogonal axes x, y, and z. Here, $R^i_{xx,0} \equiv R_{xx}(H_i = 0)$ is the base resistance and $\Delta R_{xx}(H_i) \equiv R_{xx}(H_i) - R^i_{xx,0}$ is the MR due to an applied field along the i direction. For both heterostructures, the MR is dominated by a background signal that does not depend on the magnetization direction of the MnGa or CoFeB layer. We find that the background MR mainly arises from the paramagnetic CoGa layer (see Secs. 3–5 of the Appendix). This contribution can be largely eliminated by plotting instead $\Delta R^{x-z}_{xx}/R^z_{xx,0} \equiv [R_{xx}(H_x) - R_{xx}(H_z)]/R^z_{xx,0}$ and $\Delta R^{y-z}_{xx}/R^z_{xx,0} \equiv [R_{xx}(H_y) - R_{xx}(H_z)]/R^z_{xx,0}$, as shown in Figs. 2(c) and 2(d) for the two heterostructures. The $\boldsymbol{m}$-dependent contribution of ΔR^{x-z}_{xx} and ΔR^{y-z}_{xx}, which are commonly known as anisotropic magnetoresistance (AMR) and SMR, respectively, are extracted by extrapolating the field-dependent MR contributions to zero field. Upon including the MR contribution of MnGa, $\Delta \mathrm{MR}_{\mathrm{MnGa}}$ as detailed in Sec. 4 of the Appendix, we estimate the magnitude of the SMR ratio ΔSMR, as illustrated in Figs. 2(c) and 2(d). The CoGa thickness t dependence of ΔSMR for the two heterostructures is plotted in Fig. 2(e). Assuming a transparent interface, we fit the data with an expression derived from a drift-diffusion model [11,34,35]:

$$\Delta\mathrm{SMR} = \xi^2_{\mathrm{CoGa/FM,SL}} \frac{\lambda}{t} \frac{\tanh(t/2\lambda)}{1+a} \left[1 - \frac{1}{\cosh(t/\lambda)}\right]. \quad (1)$$

We use the spin-diffusion length of CoGa λ and ξ_{SL} as the fitting parameters. $a \equiv (\rho_{\mathrm{CoGa}} t_{\mathrm{FM}})/(\rho_{\mathrm{FM}} t)$ describes the current shunting due to the presence of a conducting magnetic layer where ρ_{FM} ($\rho_{\mathrm{CoFeB}} = 120\,\mu\Omega\,\mathrm{cm}$ and $\rho_{\mathrm{MnGa}} = 196\,\mu\Omega\,\mathrm{cm}$) denotes the resistivity of the magnetic layer of thickness t_{FM}. We obtain $|\xi_{\mathrm{CoGa/MnGa,SL}}| \sim |\xi_{\mathrm{CoGa/CoFeB,SL}}| = 0.05 \pm 0.01$ and on average $\lambda \sim 1.8$ nm with the fitted curves

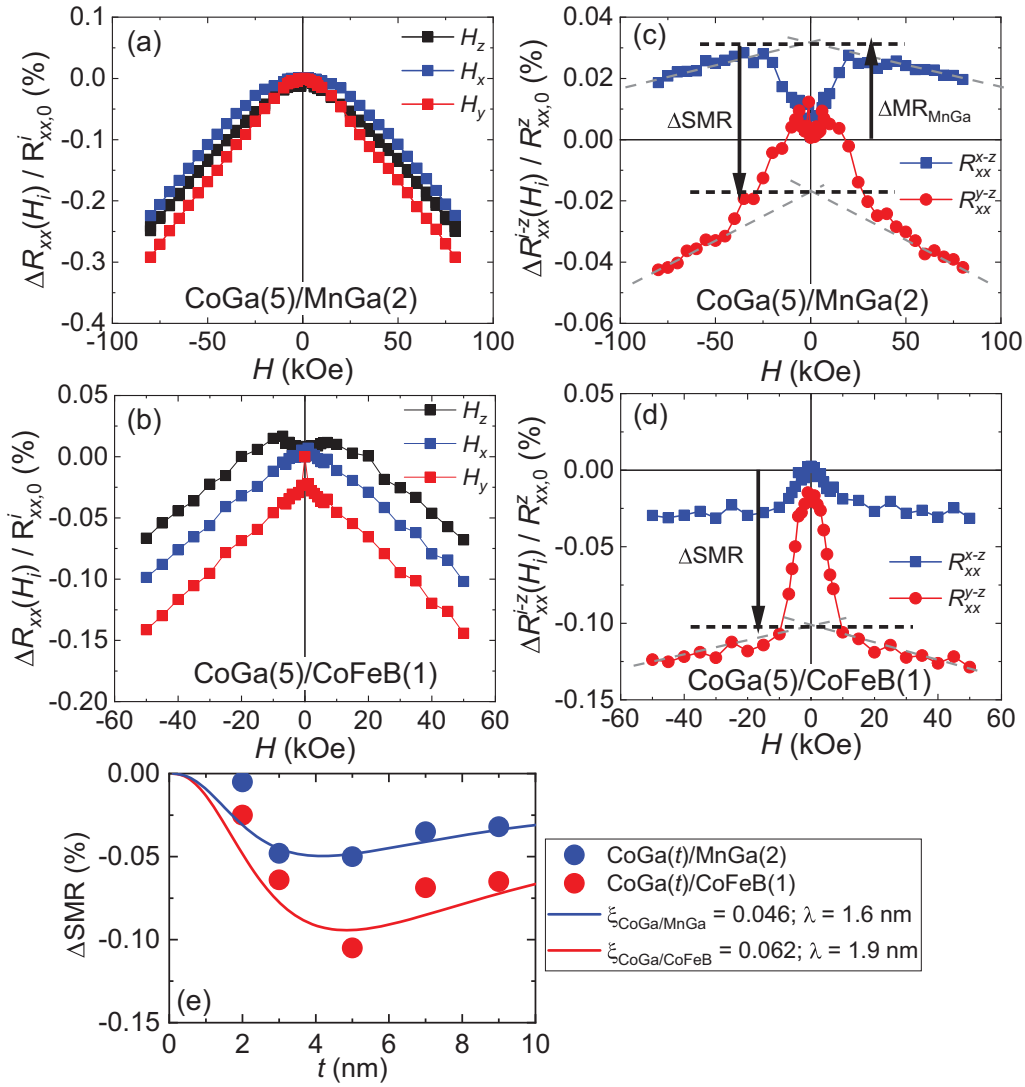

FIG. 2. Magnetoresistance as a function of three orthogonal applied fields for (a) CoGa(5)/MnGa(2) and (b) CoGa(5)/CoFeB(1) heterostructures. (c, d) $\Delta R^{x-z}_{xx}/R^z_{xx,0}$ and $\Delta R^{y-z}_{xx}/R^z_{xx,0}$, calculated from (a) and (b), respectively. Different magnetoresistance contributions are labeled. (e) CoGa thickness (t) dependence of the SMR ratio, ΔSMR. Solid lines are fits to the data using Eq. (1).

shown in Fig. 2(e). Using $\rho_{CoGa} = 175\,\mu\Omega\,\text{cm}$, we obtain a spin Hall conductivity of $143 \pm 30\,(\hbar/e)\Omega^{-1}\,\text{cm}^{-1}$. We note that the error in ξ mainly arises from the uncertainties in estimating various MR contributions that have to be subtracted from the raw data, as detailed in Secs. 3–5 of the Appendix.

D. Harmonic Hall measurements

We next quantify the Slonczewski-like ($\boldsymbol{H}_{SL} \| \boldsymbol{m} \times \boldsymbol{\sigma}$) and the field-like ($\boldsymbol{H}_{FL} \| -\boldsymbol{\sigma}$) spin-orbit effective fields in the two heterostructures using the harmonic Hall techniques [12,36–38]. Under a low-frequency sinusoidal excitation current density of amplitude J_0, the current-dependent effective fields (i.e., the SOT) modulate the direction of $\boldsymbol{m}$, thereby producing an out-of-phase second harmonic Hall resistance, $R_{2\omega}$. To estimate the effective fields, we use field scans that depend on the magnetization easy axis of the heterostructures.

For the perpendicularly magnetized CoGa(t)/MnGa(2) heterostructures, the changes of the in-phase first harmonic (fundamental) Hall resistance R_ω and $R_{2\omega}$, in response to a moderate H_x or H_y, are recorded [Fig. 3(a)]. See Sec. 6 of the Appendix for the field dependence of R_ω. Typical $R_{2\omega}$ values against H_x and H_y for a sample with $t = 5\,\text{nm}$ are plotted in Figs. 3(b) and 3(c), respectively. We define $B_x \equiv \frac{\partial R_{2\omega}(H_x)}{\partial H_x} / \frac{\partial^2 R_\omega(H_x)}{\partial H_x^2}$ and $B_y \equiv \frac{\partial R_{2\omega}(H_y)}{\partial H_y} / \frac{\partial^2 R_\omega(H_y)}{\partial H_y^2}$ to obtain the spin-orbit effective fields as follows [39]:

$$H_{SL} = -2\frac{B_x \pm 2\epsilon B_y}{1 - 4\epsilon^2}, \quad H_{FL+Oe} = -2\frac{B_y \pm 2\epsilon B_x}{1 - 4\epsilon^2}. \tag{2}$$

The $\pm$ sign corresponds to $\boldsymbol{m}$ pointing along $\pm z$. A positive H_{SL} (H_{FL+Oe}) represents $\boldsymbol{H}_{SL}$ ($\boldsymbol{H}_{FL+Oe}$) pointing along $+x(+y)$. $\epsilon(\equiv \Delta R_{PHE}/\Delta R_{xy})$ denotes the ratio of the magnitude of planar Hall effect (PHE) ΔR_{PHE} and that of the anomalous Hall effect (AHE) ΔR_{xy}. From high-field measurements,

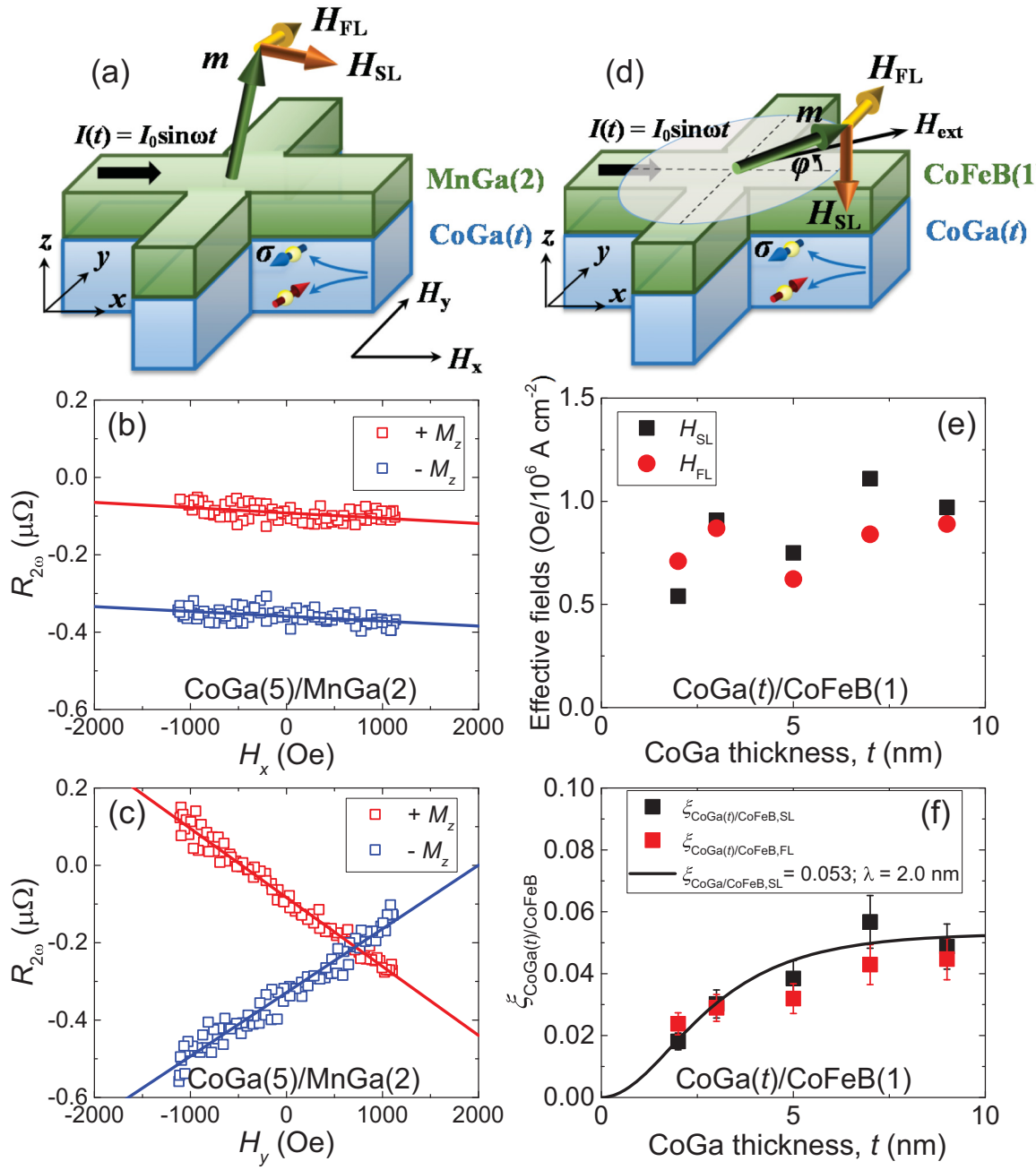

FIG. 3. (a) Schematic of the harmonic Hall measurements on the CoGa(5)/MnGa(2) bilayer with PMA. Brown and yellow arrows indicate the Slonczewski-like ($\boldsymbol{H}_{SL}$) and the fieldlike ($\boldsymbol{H}_{FL}$) spin-orbit effective field vectors, respectively, due to an applied charge current flowing along $+x$. (b), (c) $R_{2\omega}$ against an applied field along $\boldsymbol{x}$ (H_x) and along $\boldsymbol{y}$ (H_y). (d) Schematic of the harmonic Hall measurements on in-plane magnetized CoGa(t)/CoFeB(1) bilayers. (e) CoGa thickness dependence of the spin-orbit effective fields for CoGa(t)/CoFeB(1) bilayers. (f) Slonczewski-like ξ_{SL} and fieldlike ξ_{FL} spin Hall efficiencies vs t. The solid line is a fit on ξ_{SL} using Eq. (3).

we estimate $\varepsilon \sim 0.11$. Here H_{FL+Oe} includes Oersted field contribution. We evaluate the Oersted field (H_{Oe}) arising from the CoGa layer and acting on $\boldsymbol{m}$ from Ampere's law: the calculations return $H_{Oe}/J_0 \approx -0.31\,\mathrm{Oe}/10^6\,\mathrm{A\,cm^{-2}}$ for $t = 5$ nm. We subtract H_{Oe} from H_{FL+Oe} to obtain H_{FL}. Slopes of linear regressions on H_{SL} and H_{FL} against J_0 are used to evaluate the efficiencies $\xi_{SL} = \frac{2e}{\hbar}\frac{H_{SL}M_s t_{FM}}{J_0}$ and $\xi_{FL} = \frac{2e}{\hbar}\frac{H_{FL}M_s t_{FM}}{J_0}$. For $t = 5$ nm we find $\xi_{CoGa(5)/MnGa,SL} \approx +0.034 \pm 0.020$ and $\xi_{CoGa(5)/MnGa,FL} \approx +0.27 \pm 0.10$. $\xi_{CoGa(5)/MnGa,SL}$ is smaller than that estimated using the SMR method; however, this is due to the fact that a CoGa thickness of 5 nm is not large enough, compared to its spin-diffusion length ($\lambda \sim 1.8$ nm), to observe saturation of the effective field [see Fig. 3(f) and the related description below].

For in-plane magnetized CoGa(t)/CoFeB(1) bilayers, R_ω and $R_{2\omega}$ are measured as a function of the angle φ between the current flow (along $\boldsymbol{x}$) and the magnetic field applied within the film (xy) plane [Fig. 3(d)]. Details of the analyses to extract the spin-orbit effective fields are described in Sec. 7 of the Appendix. The CoGa thickness (t) dependences of H_{SL}/J_0

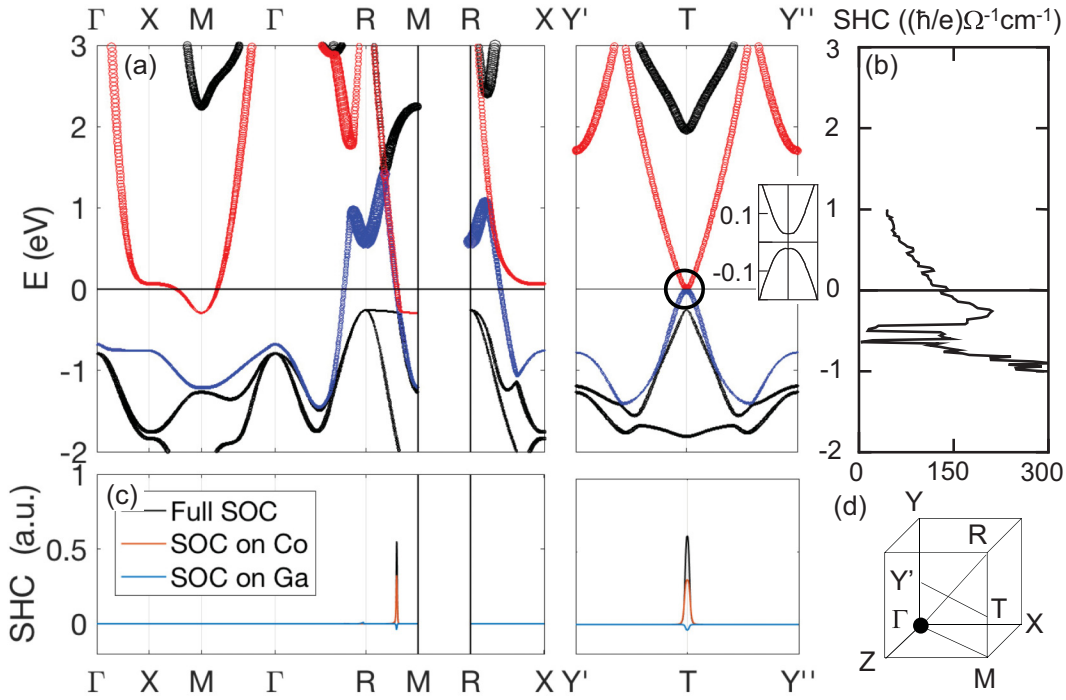

FIG. 4. (a) Band structure of β-CoGa along high-symmetry directions. $E = 0$ is the Fermi level. T, Y', and Y" points correspond to (0.5, 0.205, 0.5), (0, 0.205, 0), and (1, 0.205, 1), respectively. The two bands that cross the Fermi level are plotted in red and blue. The size of the symbols represents Ga orbital weight. We note that these two bands are degenerate along the R-M (namely R-T-M) line and cut the Fermi level at T. (b) Calculated spin Hall conductivity, SHC, against energy within a rigid band model. (c) Contributions to SHC (in arbitrary units) along the high-symmetry k path when the full SOC (black line), SOC on Co only (red line), and SOC on Ga only (blue line) is considered. (d) Illustration of the first Brillouin zone and the position of high-symmetry k points.

and H_{FL}/J_0 are plotted in Fig. 3(e). Taking into account the CoGa thickness dependence of CoFeB M_s, ranging from 1100 to 1700 emu/cm^3, the efficiencies of the Slonczewski-like ($\xi_{\mathrm{CoGa/CoFeB,SL}}$) and fieldlike ($\xi_{\mathrm{CoGa/CoFeB,FL}}$) torques are plotted in Fig. 3(f). We fit the thickness dependence with the expression [40]

$$\xi_{\mathrm{CoGa/CoFeB,SL(FL)}}(t) = \xi_{\mathrm{CoGa/CoFeB,SL(FL)}}[1 - \mathrm{sech}(t/\lambda)], \tag{3}$$

which gives $\xi_{\mathrm{CoGa/CoFeB,SL}} = +0.053$ and $\lambda = 2.0$ nm, in satisfactory agreement with the SMR method. In addition, we have also carried out spin-torque ferromagnetic resonance and modulation of damping measurements [40] for quantifying the sign and the magnitude of SOT in the CoGa(5)/CoFeB(1) bilayer, as detailed in Sec. 8 of the Appendix. Results are in agreement with those obtained using the harmonic Hall method.

We find $\xi_{\mathrm{CoGa/CoFeB,FL}}$ similar in magnitude with $\xi_{\mathrm{CoGa/CoFeB,SL}}$. Interestingly, ξ_{SL} is similar in magnitude for both bilayers CoGa/MnGa and CoGa/CoFeB, whereas ξ_{FL} is significantly larger for the former. These results suggest that SOT and ξ sensitively depend on the interfacial band matching, i.e., the interface transparency. The exceptionally large $\xi_{\mathrm{CoGa/MnGa,FL}}$ may originate from contributions due to the Rashba-Edelstein effect [1,37,41], fieldlike component of the spin-transfer torque due to the spin Hall induced spin current [42–45], spin swapping torques [46], and other interfacial effects [47,48].

III. FIRST-PRINCIPLES CALCULATIONS

It is commonly believed that the SOC, scaling with Z^4 (Z = atomic number), is an essential ingredient for obtaining large SOT. However, our observations on a CoGa compound that contains no heavy element and yet exhibits appreciable SHE at room temperature challenge this archetypal assumption. The relatively high $\rho_{\mathrm{CoGa}} = 175\,\mu\Omega\,\mathrm{cm}$ with an estimated mean free path l comparable to twice the lattice spacing $d \sim 2.8$ Å (see Sec. 9 of the Appendix) in general excludes interpretation based on extrinsic spin-dependent skew scattering. In order to gain insights into the mechanism of spin current generation in CoGa, we perform first-principles calculations (see Sec. 10 of the Appendix for the details) based on density-functional theory to study the *intrinsic* SHC of stoichiometric β-CoGa [49]. Note that the first-principles calculations find the ground state of stoichiometric β-CoGa to be paramagnetic.

The band structure along high-symmetry k paths and the corresponding SHC contributions at the Fermi level E_F (i.e., at $E = 0$) are plotted in Figs. 4(a) and 4(c), respectively. Due to the strong orbital hybridization, bands with mainly Co d character are pushed down to lower energy below E_F while the Ga sp states are moved above, leaving only two bands that cross E_F at several k points: the two bands are color coded with red and blue. To illustrate the degree of orbital hybridization, the character of the band is represented by the symbol size: large-size (small-size) symbols indicate bands with strong Ga (Co) character. The right panel

of Fig. 4(a) shows the highly dispersive $3d$-$4p$ hybridized bands along the R-M line that cut E_F at the T point with $(k_x, k_y, k_z) \sim (0.5,\ 0.205,\ 0.5)$. When no SOC is included, two bands are degenerate because the R-M line possesses C_{4v} symmetry along the k_y axis. Upon introducing the SOC, the band degeneracy is lifted, which gives rise to a small energy gap and large SHC contributions (i.e., spin Berry curvature) in the vicinity of the T point [Fig. 4(c)]. By integrating the SHC contributions over all occupied states in the k space, we obtain a calculated SHC of $+140\,(\hbar/\mathrm{e})\,\Omega^{-1}\,\mathrm{cm}^{-1}$. The energy dependence of SHC is plotted in Fig. 4(b). Within a rigid band model, these results suggest that large SHC appears throughout the aforementioned dispersive bands, with a local SHC maximum being located at $E \sim -0.25\,\mathrm{eV}$.

The d-p hybridized bands play an essential role in generating the SHC in β-CoGa. To display the importance of orbital hybridization, the SHC of a hypothetical $B2$-Co and $B2$-Ga, which are the bcc phases of Co and Ga, respectively, are calculated using first-principles calculations. Note that bcc Co and bcc Ga are not the most stable phases. The integrated spin Hall conductivities of bcc Co and bcc Ga are -4 and $-220\,(\hbar/\mathrm{e})\,\Omega^{-1}\,\mathrm{cm}^{-1}$, respectively. Both the sign and magnitude of SHC change upon forming the alloy phase (CoGa). The orbitals responsible for generating the SHC for the bcc Co and bcc Ga are the d and sp states, respectively. Since the strength of the spin-orbit coupling of the Co and Ga atoms does not change upon forming the alloy, the change in SHC can be attributed to the formation of the p-d hybridized bands that cross E_F.

To identify the role of the spin-orbit coupling of each element, we have calculated the integrated spin Hall conductivity of the CoGa alloy when the spin-orbit coupling of either Co or Ga is turned off. The corresponding SHC contributions along the chosen k path are plotted in Fig. 4(c). The integrated SHC without the Ga (Co) spin-orbit coupling is $+101.4\,(\hbar/\mathrm{e})\,\Omega^{-1}\,\mathrm{cm}^{-1}$ $[+40.5\,(\hbar/\mathrm{e})\,\Omega^{-1}\,\mathrm{cm}^{-1}]$. The sum of the two values is close to the SHC of CoGa when the spin-orbit couplings of both atoms are turned on. These results show that the contribution of element spin-orbit coupling to the integrated SHC is simply additive and that the effect is larger for Co. Finally, we emphasize that the formation of the pseudogap [see Fig. 4(a) inset] near E_F leads to reduction in the longitudinal conductivity [50] and thus increases the spin Hall angle of CoGa (even though the spin Hall conductivity is not particularly large, the spin Hall angle, when it is of intrinsic origin, can be increased by reducing the longitudinal conductivity).

In an attempt to provide interpretation on the origin of the SHC in CoGa, we examine, on the basis of the linear response theory, the expression of the intrinsic SHC, $\sigma_{yx}^{\mathrm{SH}}$:

$$\sigma_{yx}^{\mathrm{SH}} = \sum_{\boldsymbol{k}} \sum_{n \neq n'} \frac{2\mathrm{Im}[\langle \mathbf{k}n|j_y|\mathbf{k}n'\rangle\langle \mathbf{k}n'|v_x|\mathbf{k}n\rangle]}{(\varepsilon_{\mathbf{k}n} - \varepsilon_{\mathbf{k}n'})^2}. \tag{4}$$

Here, $j_y = 1/2(s_z v_y + v_y s_z)$ is the spin current operator, $v_{x(y)}$ is the velocity operator, s_z is the z component of the Pauli matrix, and $\varepsilon_{\mathbf{k}n}$ and $\varepsilon_{\mathbf{k}n'}$ are eigenvalues of the occupied $|\mathbf{k}n\rangle$ and unoccupied $|\mathbf{k}n'\rangle$ states, respectively. The velocity matrix elements in the numerator may lead to a selection rule [51] which allows transitions between the $|\mathbf{k}n\rangle$ and $|\mathbf{k}n'\rangle$ states that satisfy $l = l' \pm 1$ and $m = m' \pm 1$ for the angular quantum and magnetic quantum numbers, respectively. In the $5d$ elements, the bands crossing the Fermi level are, in general, mostly d orbitals with less p character: thus the transitions typically involve the d orbitals. In contrast, for CoGa, the transitions between different l orbitals contribute to the SHC due to the hybridized p-d character of the bands near the Fermi level. For example, in the vicinity of the T point in Fig. 4, transition from the d_{-1} state $(l = 2, m = -1)$ to the p_0 state $(l = 1,\ m = 0)$ [51], corresponding to $l = l' + 1$ and $m = m' - 1$, gives a large positive contribution to the SHC. We emphasize that the main consequence of the p-d hybridization is the redistribution of the p and d orbital occupation inside the Co and Ga atoms. As a result, the transition amplitude between different orbitals within the Co and Ga atom changes.

IV. CONCLUSION

Recently, strong intrinsic AHE and SHE have been predicted in another heavy-element-free compound Mn_3Ge where the nonvanishing Berry curvatures are attributed to the frustrated triangular lattice [52–54]. Here, using CoGa as an example, we establish the critical role of d–p orbital hybridization for obtaining highly dispersive hybridized bands at E_F that exhibit large intrinsic SHC, without necessarily invoking heavy elements with strong SOC. The good agreement between the calculated SHC and the SHC obtained from the experiments suggests that the intrinsic mechanism may be dominant, although we cannot completely rule out possible contributions from extrinsic effects due to, e.g., surface/interface scattering.

The appreciable spin Hall effect in CoGa together with its unique capability for stabilizing an ultrathin MnGa with strong PMA in CoGa/MnGa/oxide heterostructures allows realization of magnetic switches and oscillators with significantly higher thermal stability and operating speed than the common Ta/CoFeB/MgO structure. The anisotropy and the resonance frequency of MnGa can be easily tuned by varying the Mn:Ga ratio [55] or by chemical substitution [56–59], thus providing an attractive solution for bridging the "terahertz gap." Moreover, we expect further enhancement of the competitiveness of our structure by combining SOT-induced switching with voltage-controlled magnetic anisotropy at the MnGa/oxide interface.

ACKNOWLEDGMENTS

We would like to thank S. Mitani for technical help. This work was partly supported by Japan Society for the Promotion of Science (JSPS) Grant-in-Aids for Specially Promoted Research (Grant No. 15H05702); Ministry of Education, Culture, Sports, Science, and Technology Research and Development Next-Generation Information Technology; and Innovation and Spintronics Research Network of Japan. Computations were partly performed at Research Institute for Information Technology, Kyushu University. Y.-C.L. is supported by JSPS International Fellowship for Research in Japan (Grant No. JP17F17064).

Y.-C.L. and H.L. contributed equally to this work.

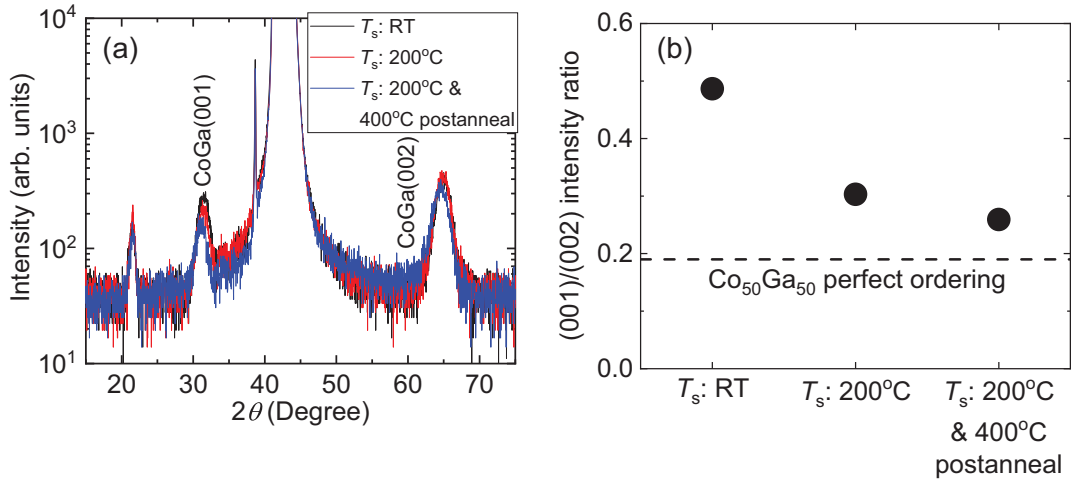

FIG. 5. (a) X-ray-diffraction spectra of CoGa(5)/CoFeB(1) bilayers with CoGa grown under different conditions. (b) Comparison between the experimental (001)/(002) intensity ratio and that expected from a fully ordered CoGa.

APPENDIX

1. Sample fabrication and characterizations

All films are grown on MgO(001) substrates in an ultrahigh-vacuum chamber by magnetron sputtering. CoGa layers are deposited at substrate temperature (T_s) of 200 °C and postannealed at 400 °C for obtaining $B2$ structure, unless otherwise stated. See Sec. 2 of the Appendix for how the ordering varies with the substrate temperature during deposition. The remaining layers are grown at ambient temperature. The top Ta(1) layer is fully oxidized and is considered to be insulating. Hall bar devices with a nominal channel width of 10 μm and a length of 25 μm between the Hall probes for measuring longitudinal resistance are fabricated by standard optical lithography and Ar ion milling. Ta(5)/Au(100) are grown by sputtering for electrical contact.

Magnetic properties of unpatterned films are measured by a SQUID vibrating-sample magnetometer (VSM) with a maximum field of 70 kOe or a VSM with a maximum field of 20 kOe. X-ray-diffraction spectra are measured using a Cu Kα source in parallel beam configuration and with a graphite monochromator on the detector side.

In current-induced switching experiments, a dc current is swept using a source meter and the Hall voltage is measured with a nanovoltmeter. Magnetotransport properties are characterized in a physical properties measurement system. The temperature is varied from 2 to 400 K with an applied field up to 140 kOe. For harmonic Hall measurements, a sinusoidal signal of constant amplitude and frequency of 512.32 Hz is applied using a low distortion function generator. The first- and second-harmonic Hall voltages are measured with two lock-in amplifiers. The root-mean-square current of the circuit is estimated by measuring the voltage drop across a 100-Ω series resistor using a third lock-in amplifier. The hard-axis anisotropy field of the MnGa with PMA is estimated from the curvature of R_{xy} as a function of an in-plane applied field.

2. Ordering parameter of $B2$ β-CoGa

In $B2$ structure, the ordering is given by the differentiation of atomic occupancy on 1a (0, 0, 0) and 1b (0.5, 0.5, 0.5) sites [Fig. 1(b)]. The ordering can be revealed by comparing the x-ray-diffraction intensity ratio of superlattice peaks, e.g., (001) and the fundamental (002) diffraction peaks. In a

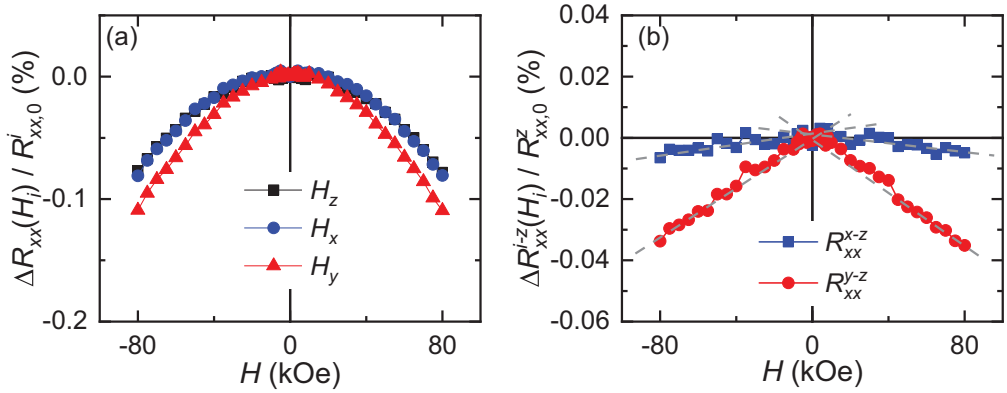

FIG. 6. $\Delta R_{xx}(H_i)/R^i_{xx,0}$ (a) and $\Delta R^{i-z}_{xx}(H_i)/R^z_{xx,0}$ (b) as a function of applied field H_i along x, y, and z directions at $T = 295$ K for CoGa(5) layer.

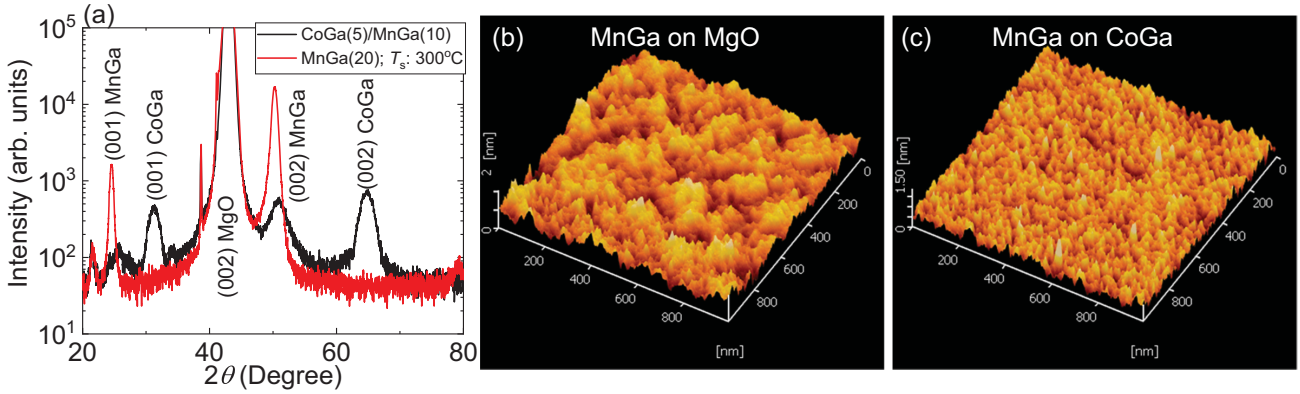

FIG. 7. (a) θ-2θ x-ray-diffraction spectra of CoGa(5)/$Mn_{1.44}$Ga(10) (black) and $Mn_{1.44}$Ga(20) (red) grown on MgO substrates. (b), (c) AFM micrographs of the two samples.

perfectly ordered equiatomic $Co_{50}Ga_{50}$ compound, a moderate (001)/(002) intensity ratio of ∼0.2 is expected, due to the small difference in atomic number Z between Co and Ga [Z(Co) ∼59 and Z(Ga) ∼ 69.7]. In a fully disordered bcc crystal, with no difference in atomic occupancy on 1a and 1b sites, the (001) reflection is forbidden and the (001)/(002) intensity ratio is zero. The ordering parameter S is given by the following expression:

$$S = \sqrt{\frac{(001)/(002)\text{ratio}_{\text{exp}}}{(001)/(002)\text{ratio}_{\text{cal}}}}. \quad \text{(A1)}$$

If the vacancy formation at 1a is allowed, it can be regarded as a third species with Z(vacancy) = 0 and with *unknown* concentration. It largely increases the atomic contrast between the two sites and can give rise to an intensity ratio >0.2. However, for a given experimental (001)/(002) ratio, there will be no unique solution of the corresponding atomic ordering, without knowing the concentration of the vacancy.

Figure 5(a) shows the symmetrical θ-2θ x-ray-diffraction spectra of three CoGa(5)/CoFeB(1) samples with different CoGa growth conditions: growth at room temperature, growth at 200 °C (i.e., T_s = 200 °C), and the optimized growth at

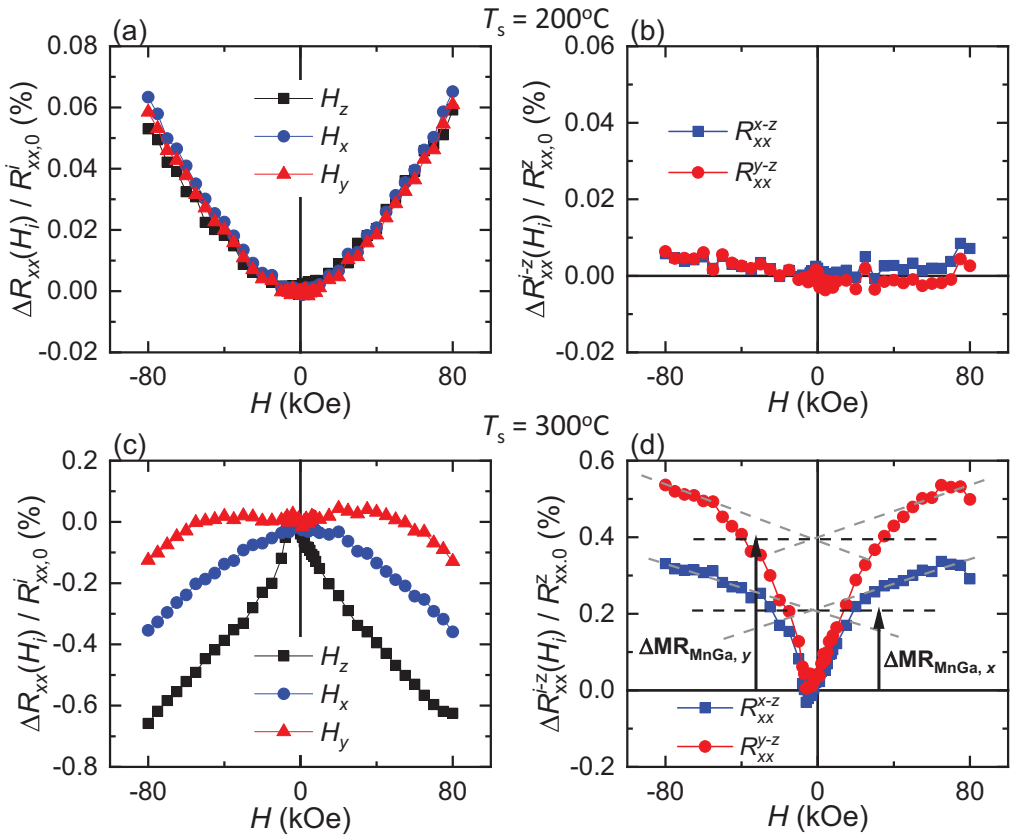

FIG. 8. $\Delta R_{xx}(H_i)/R_{xx,0}^{i}$ (a), (c) and $\Delta R_{xx}^{i-z}(H_i)/R_{xx,0}^{z}$ (b), (d) as a function of applied field H_i along x, y, and z directions. Results for MnGa(20) films being deposited at substrate temperatures of T_s = 200 °C (a), (b) and T_s = 300 °C (c), (d) are compared. Note that the scales of the upper and lower panels differ by a factor of 10.

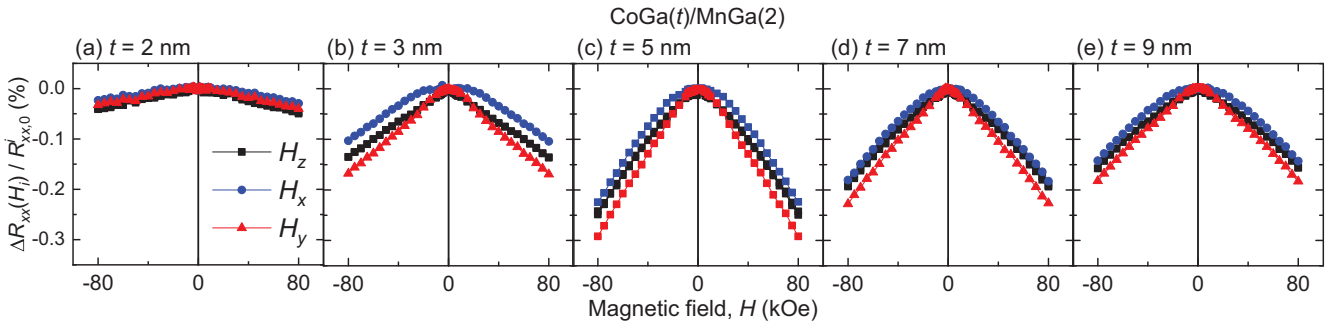

FIG. 9. Field dependence of $\Delta R_{xx}(H_i)/R^i_{xx,0}$ for CoGa(t)/MnGa(2) heterostructures with t varying from 2 to 9 nm.

200 °C followed by postannealing at 400 °C for 30 min. The three samples exhibit similar (002) peak intensity, which indicates that their crystallinity is comparable, whereas the evolution of (001) peak intensity reveals the change of ordering parameter. The experimental (001)/(002) peak intensity ratios are plotted in Fig. 5(b). The data are all higher than the calculated intensity ratio of perfect $Co_{50}Ga_{50}$ (dashed horizontal line), which suggests in all samples the presence of vacancy. The density of vacancy in CoGa crystallites decreases upon introducing thermal treatment. We estimate that the optimized $Co_{53}Ga_{47}$ films used in this paper may contain up to 10% vacancy on the 1*a* site and with ∼10% of 1*b* site being occupied by Co, in lieu of Ga.

3. Magnetoresistance of CoGa(5)/MAO(2)/Ta(1) heterostructure

We measure the longitudinal resistance R_{xx} of a MgO(001) substrate/CoGa(5)/MAO(2)/Ta(1) stack as a function of applied field H_i along three orthogonal directions: $i = x$ (in-plane parallel to current), $i = y$ (in-plane transverse to current), and $i = z$ (out-of-plane transverse to current). As defined above, $\Delta R_{xx}(H_i) \equiv R_{xx}(H_i) - R^i_{xx,0}$ and $\Delta R^{i-z}_{xx}(H_i) \equiv R_{xx}(H_i) - R_{xx}(H_z)$ where $R^i_{xx,0} \equiv R_{xx}(H_i = 0)$ is the base resistance. $\Delta R_{xx}(H_i)/R^i_{xx,0}$ and $\Delta R^{i-z}_{xx}(H_i)/R^z_{xx,0}$ are plotted as a function of applied field H_i at $T = 295$ K in Figs. 6(a) and 6(b), respectively. The CoGa single layer exhibits negative MR in all directions with quadraticlike field dependence. In addition, there is a small directional MR anisotropy of the form $R_{xx}(H_x) \sim R_{xx}(H_z) > R_{xx}(H_y)$ that does not saturate at 80 kOe. From Fig. 6(b), $\Delta R^{y-z}_{xx}(H)$ is essentially linear with H whereas $\Delta R^{x-z}_{xx} \approx 0$. Although we do not know the origin of this MR contribution, we argue that it may contain contribution from Hanle magnetoresistance (HMR) [60], which has the same field directional dependence but scales with H^2. The minor contribution from HMR is understood from the magnitude of the observed MR (∼4×10^{-4} at 80 kOe), being significantly higher than the reported HMR values in YIG/Pt(7) (∼6×10^{-5} at 90 kOe) or SiO_2/Ta(5) (∼4.5×10^{-6} at 90 kOe) structures [60].

We perform linear extrapolation of $\Delta R^{y-z}_{xx}(H)$ and $\Delta R^{x-z}_{xx}(H)$ from high fields to zero field as shown in Fig. 6(b). The two y intercepts $R^{x-z}_{xx,0}$ and $R^{y-z}_{xx,0}$ practically coincide with the origin of the graph. We will apply this protocol hereafter on CoGa/FM bilayer systems (Sec. 5 of the Appendix) in order to eliminate the field-dependent MR contribution from CoGa.

4. Characterizations of MnGa(20)/MAO(2)/Ta(1) heterostructure

It is not trivial to extract the magnetotransport contribution of MnGa grown on the CoGa seed layer for two reasons. First, the MR of tetragonal MnGa with PMA depends sensitively on the atomic ordering of the compound. Second, to date, no insulating seed layer or substrate is known to promote the growth of MnGa of comparable quality with that grown on the CoGa seed layer, under similar growth conditions. We grow thick (thickness ∼20 nm) MnGa films directly on MgO substrates at elevated substrate temperature (T_s), in an attempt to mimic the MR behavior of high-quality 2-nm MnGa grown on the CoGa seed layer at ambient temperature. At $T_s = 200$ °C, the resulting MnGa film is practically nonmagnetic. At $T_s =$

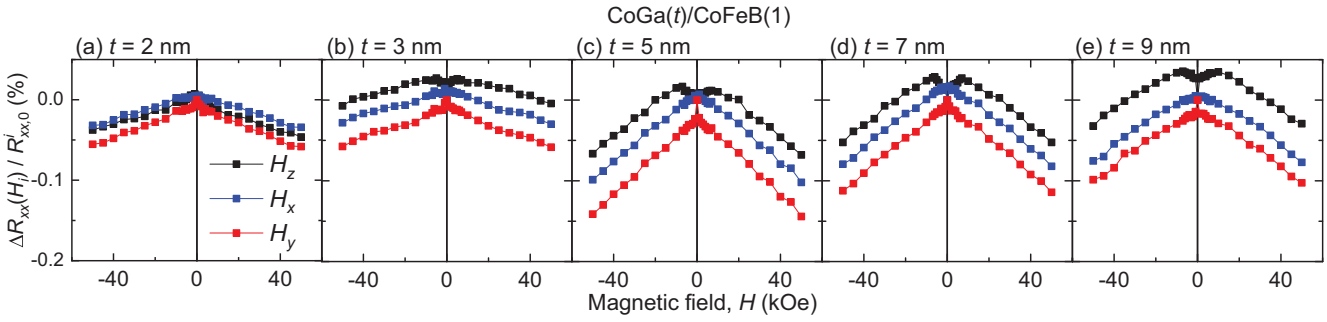

FIG. 10. Field dependence of $\Delta R_{xx}(H_i)/R^i_{xx,0}$ for CoGa(t)/CoFeB(1) heterostructures with t varying from 2 to 9 nm.

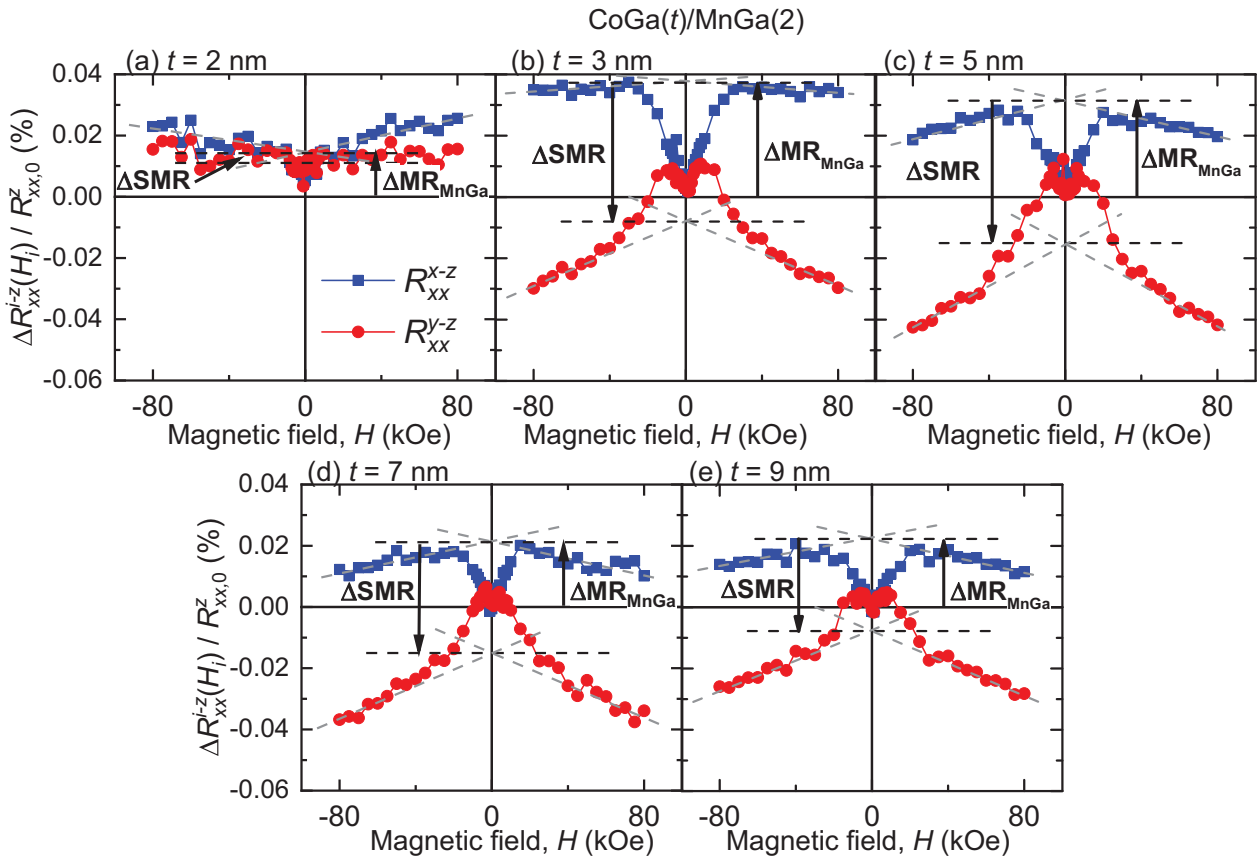

FIG. 11. CoGa thickness (t) dependence of $\Delta R^{i-z}_{xx}(H_i)/R^{z}_{xx,0}$ as a function of applied field H_i for CoGa(t)/MnGa(2) samples. Contributions of $\Delta\mathrm{MR}_{\mathrm{MnGa}}$ and ΔSMR are shown for each thickness.

300 °C, the MnGa film starts to crystallize and exhibits PMA. Further increase of the substrate temperature improves the MnGa crystallinity but degrades the wetting and eventually leads to islandlike insulating films. The XRD spectra and the atomic force microscopy (AFM) micrographs of MnGa grown on MgO at $T_s = 300$ °C and on CoGa are compared in Fig. 7. MnGa grown on MgO exhibits better crystallinity with a higher c lattice parameter compared to MnGa grown on CoGa. From the AFM, the grains of MnGa grown on MgO appear to be larger but it is difficult to predict how these differences will manifest in the transport properties.

The field-dependent MR measurements of MgO(001) substrate/MnGa(20)/MAO(2)/Ta(1) heterostructures are plotted in Figs. 8(a) and 8(b) and Figs. 8(c) and 8(d) for samples prepared at $T_s = 200$ and 300 °C, respectively. MnGa grown at $T_s = 200$ °C exhibits weak positive MR with a quadratic field dependence and a very small field directional anisotropy $<0.01\%$, as shown in Fig. 8(b). In contrast, MnGa grown at $T_s = 300$ °C shows negative MR that strongly depends on the field directions. The MR is the form $R_{xx}(H_y) > R_{xx}(H_x) > R_{xx}(H_z)$. We define $\Delta\mathrm{MR}_{\mathrm{MnGa},i}$ as the zero-field MR contribution of MnGa upon extrapolating $\Delta R^{i-z}_{xx}(H)$ from high field. We obtain $\Delta\mathrm{MR}_{\mathrm{MnGa},y} \approx 2 \times \Delta\mathrm{MR}_{\mathrm{MnGa},x}$. A possible source of $\Delta\mathrm{MR}_{\mathrm{MnGa}}$ is the tetragonal lattice of MnGa which naturally leads to transport anisotropy between in-plane (H_x and H_y) and out-of-plane (H_z) field directions. Based on the resistivity and the magnetic properties, we consider that the MnGa film grown at $T_s = 300$ °C is the closest, in terms of transport properties, to the MnGa film grown on the CoGa seed layer. For simplicity, we will assume hereafter $\Delta\mathrm{MR}_{\mathrm{MnGa},y} \approx \Delta\mathrm{MR}_{\mathrm{MnGa},x} \equiv \Delta\mathrm{MR}_{\mathrm{MnGa}}$ in CoGa/MnGa bilayers. We will discuss the consequences of such an assumption in Sec. 5 of the Appendix.

5. Extraction of SMR ratio ΔSMR in CoGa(t)/FM bilayer systems

The field dependences of $\Delta R_{xx}(H_i)/R^{i}_{xx,0}$ for CoGa(t)/MnGa(2) and CoGa(t)/CoFeB(1) heterostructures are plotted in Figs. 9 and 10, respectively. For the CoGa(t)/CoFeB(1) series, the nonsaturating MR at high field is mainly arising from that of the CoGa layer (see Sec. 3 of the Appendix). For the CoGa(t)/MnGa(2) series, the stronger high-field MR agrees with the additive MR contributions from the CoGa and MnGa layers.

This high-field quasi-isotropic MR can be largely eliminated by plotting $\Delta R^{i-z}_{xx}(H_i)/R^{z}_{xx,0}$ as a function of applied field H_i for CoGa(t)/MnGa(2) samples, as shown in Fig. 11. We are interested in the MR contributions that depend on the magnetization direction of adjacent MnGa, which can be extracted by extrapolating the data from high field to zero field. We define $R^{i-z}_{xx,0}$ as the resulting y intercept from the linear extrapolation. Following Sec. 3 and Sec. 4 of the

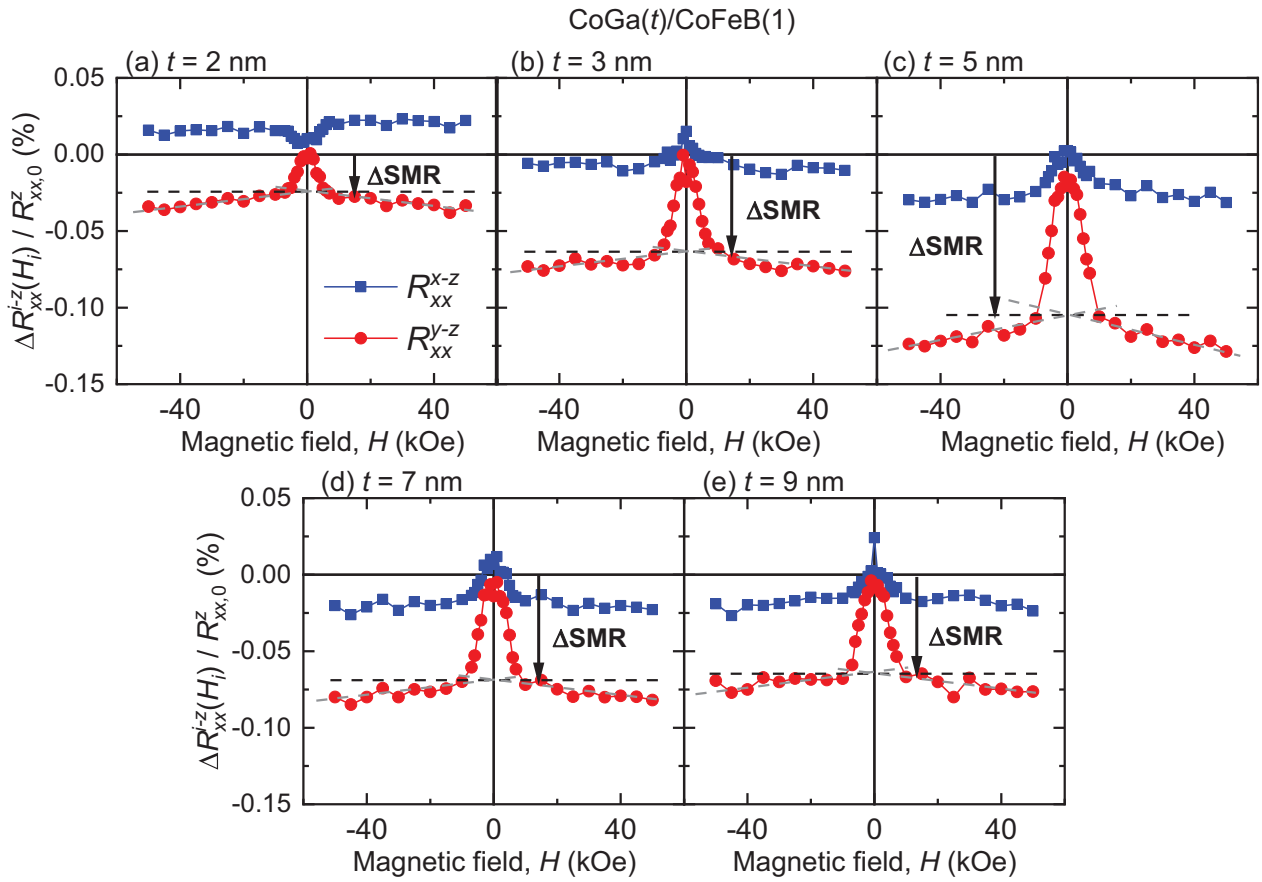

FIG. 12. CoGa thickness (t) dependence of $\Delta R_{xx}^{i-z}(H_i)/R_{xx,0}^{z}$ as a function of applied field H_i for CoGa(t)/CoFeB(1) samples. The ΔSMR contribution is shown for each CoGa thickness.

Appendix, we consider

$$R_{xx,0}^{x-z} = \Delta\mathrm{MR}_{\mathrm{MnGa}}, \tag{A2}$$

$$R_{xx,0}^{y-z} \approx \Delta\mathrm{MR}_{\mathrm{MnGa}} + \Delta\mathrm{SMR}. \tag{A3}$$

Since $\Delta\mathrm{MR}_{\mathrm{MnGa},y}$ is positive and is likely to be larger than $\Delta\mathrm{MR}_{\mathrm{MnGa},x}$, we tend to underestimate the size of ΔSMR, which is negative.

$\Delta R_{xx}^{i-z}(H_i)/R_{xx,0}^{z}$ is plotted as a function of applied field H_i for CoGa(t)/CoFeB(1) samples in Fig. 12. For simplicity, we consider

$$R_{xx,0}^{x-z} \approx \Delta\mathrm{AMR}, \tag{A4}$$

$$R_{xx,0}^{y-z} \approx \Delta\mathrm{SMR}. \tag{A5}$$

ΔSMRs for each CoGa thickness are shown in Fig. 12. If $\Delta\mathrm{MR}_{\mathrm{MnGa},y} \approx 2\Delta\mathrm{MR}_{\mathrm{MnGa},x}$ is considered, the SMR of the CoGa/MnGa system will be slightly higher because both $\Delta\mathrm{MR}_{\mathrm{MnGa},y}$ and $\Delta\mathrm{MR}_{\mathrm{MnGa},x}$ are positive. The estimated SMRs for the two cases are plotted in Fig. 13 against the CoGa thickness t: black squares represent the same data as shown in Fig. 2(e) and red circles show the ΔSMR obtained from $\Delta\mathrm{MR}_{\mathrm{MnGa},y} \approx 2\Delta\mathrm{MR}_{\mathrm{MnGa},x}$. We find that ξ (and λ) changes slightly but remains in agreement (within the experimental error) with our overall estimation $\xi = 0.05 \pm 0.01$.

We also note that for $t \geqslant 3$ nm the negative sign of $R_{xx,0}^{x-z}$ is inconsistent with the positive AMR of CoFeB [34]. The origin of this unconventional negative AMR is unclear for the moment. We speculate that the unintentional intermixing at the CoGa/CoFeB interface during the growth may have formed an alloy with different magnetotransport properties, compared to CoGa and CoFeB alone.

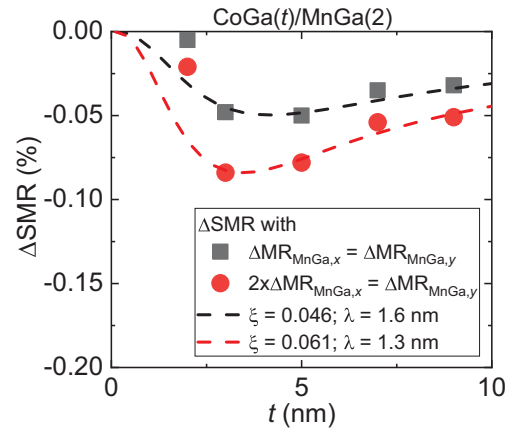

FIG. 13. CoGa thickness (t) dependence of the SMR ratio, ΔSMR, from two analysis methods. Solid lines are fits to the data using Eq. (1).

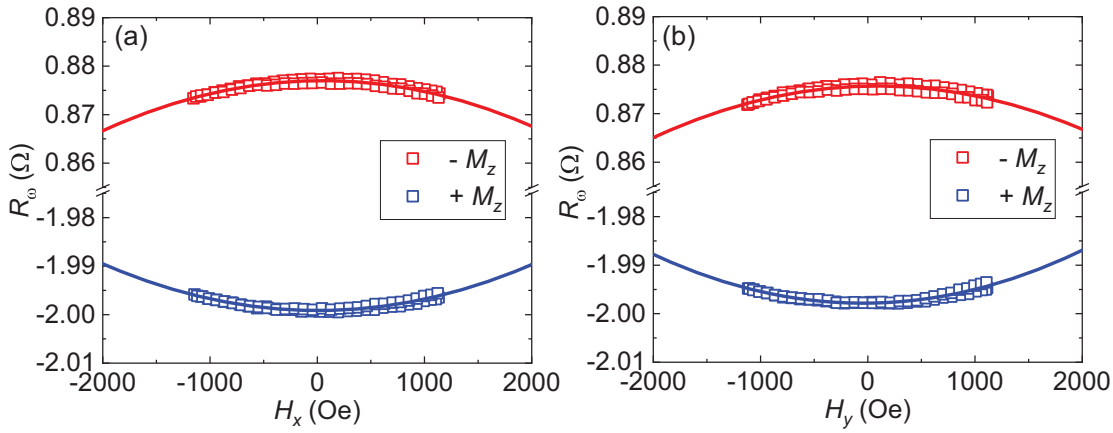

FIG. 14. (a), (b) R_ω plotted against an applied field along $\boldsymbol{x}$ (H_x) (a) and along $\boldsymbol{y}$ (H_y) (b). Solid lines are quadratic fits to the experimental data.

6. Harmonic Hall measurement for out-of-plane magnetized CoGa(t)/MnGa

In Fig. 14, we plot the first-harmonic signal R_ω measured simultaneously with the $R_{2\omega}$ signal presented in Figs. 2(b) and 2(c). The data are fitted by a quadratic function $bH^2 + {R_\omega}^0$ where b and ${R_\omega}^0$ are the fitting parameters. We define $\Delta R_\omega \equiv R_\omega^0(+M_z) - R_\omega^0(-M_z)$. In the limit of small tilting angle (i.e., $H \ll H_k$), the anisotropy field H_k can be expressed as [61] $H_k = \sqrt{|\frac{\Delta R_\omega}{4b}|}$. We obtain $H_k \sim 19$ kOe, which is in good agreement with the H_k estimation from the VSM. Although MnGa is a ferrimagnet, it seems reasonable to describe its magnetic properties using a simple macrospin model with an effective net M_s of MnGa.

7. Harmonic Hall measurement for in-plane magnetized CoGa(t)/CoFeB

We extract the current-induced spin-orbit effective fields from the angular dependence of $R_{2\omega}$, as described by Avci *et al.* [38]. Here we consider the case where both the external field $\boldsymbol{H}_{\rm ext}$ and the magnetization vector $\boldsymbol{m}$ lie in the (xy) plane, i.e., the polar angle $\theta = 90^\circ$. The expressions of the harmonic Hall resistances are of the form

$$R_\omega = R_{\rm AHE}\cos\theta + R_{\rm PHE}\sin^2\theta\sin 2\varphi, \tag{A6}$$

$$\begin{aligned} R_{2\omega} &= -\left(R_{\rm AHE}\frac{H_{\rm SL}}{H_{\rm ext}+H_k} + R^0_{\nabla T}\right)\cos\varphi \\ &\quad + 2R_{\rm PHE}(2\cos^3\varphi - \cos\varphi)\frac{H_{\rm FL}+H_{\rm Oe}}{H_{\rm ext}} \\ &\equiv R_{\rm SL} + R_{\rm FL+Oe} + R_{\nabla T}, \end{aligned} \tag{A7}$$

where $R_{\rm SL}$, $R_{\rm FL+Oe}$, and $R_{\nabla T}$ are the Slonczewski-like effective field, the fieldlike effective field plus the Oersted field, and the thermoelectric contribution to $R_{2\omega}$, respectively. $R_{\rm AHE}$, $R_{\rm PHE}$, and H_k denote the anomalous Hall resistance, the planar Hall resistance, and the anisotropy field of the CoFeB layer. Typical $R_\omega(\varphi)$ and $R_{2\omega}(\varphi)$ for a CoGa(5)/CoFeB(1)/MAO(2)/Ta(1) film measured with $H_{\rm ext} =$ 1300 Oe are plotted in Figs. 15(a) and 15(b). The prefactor of the "$\cos\varphi$" component can be extracted by fitting $R_{2\omega}(\varphi)$ to a $\cos\varphi$ function at $\varphi = 45$, 135, 225, and 315°, where at these particular points the "$2\cos^3\varphi - \cos\varphi$" component vanishes. Then, upon subtracting the "$\cos\varphi$" contribution from $R_{2\omega}(\varphi)$, we fit the data with a $2\cos^3\varphi - \cos\varphi$ function. A decomposition of $R_{2\omega}(\varphi)$ into the two contributions is shown in Fig. 15(c). We note that the antisymmetric component of the raw $R_{2\omega}(\varphi)$ data, which mainly arises from the sample misalignment, is very low.

Based on Eq. (A7), the prefactor of the $\cos\varphi$ component may contain a thermoelectric contribution $R^0_{\nabla T}$ that does not depend on $H_{\rm ext}$. We measure $R_{2\omega}(H_{\rm ext})$ with the field applied along $\varphi = 45$ and 225°. $R_{2\omega}$ is plotted against $\frac{1}{H_k+|H_{\rm ext}|}$ in Fig. 15(d): a relatively small $R^0_{\nabla T}$ is found from the y intercept, which will increase $H_{\rm SL}$ by ~10%.

8. Spin-torque FMR and modulation of damping measurements for in-plane magnetized CoGa(5)/CoFeB(1)

We carry out spin-torque ferromagnetic resonance (ST-FMR) [40] measurement as an independent verification of the magnitude and the sign of the spin-orbit torques in the CoGa/CoFeB bilayer. A microwave excitation and a dc bias are applied simultaneously via a bias tee to the device consisting of a bar with a length of 50 μm and a width of 10 μm. The microwave signal is further modulated by a square wave at a frequency of 512.32 Hz and the resulting mixing voltage $V_{\rm mix}$ at the modulated frequency is measured using a lock-in amplifier. A typical ST-FMR spectrum of the in-plane magnetized CoGa(5)/CoFeB(1) bilayer is shown in Fig. 16(a). The raw data are fitted by the sum of a symmetric Lorentzian and an antisymmetric Lorentzian with prefactors S and A, respectively:

$$V_{\rm mix} = S\frac{\Delta^2}{\Delta^2 + (H_{\rm ext}-H_{\rm FMR})^2} + A\frac{\Delta\,(H_{\rm ext}-H_{\rm FMR})}{\Delta^2 + (H_{\rm ext}-H_{\rm FMR})^2}. \tag{A8}$$

Δ, $H_{\rm ext}$, and $H_{\rm FMR}$ are the resonance linewidth, the external field, and the resonance field, respectively. The symmetric Lorentzian component (blue line in Fig. 16) is attributed to

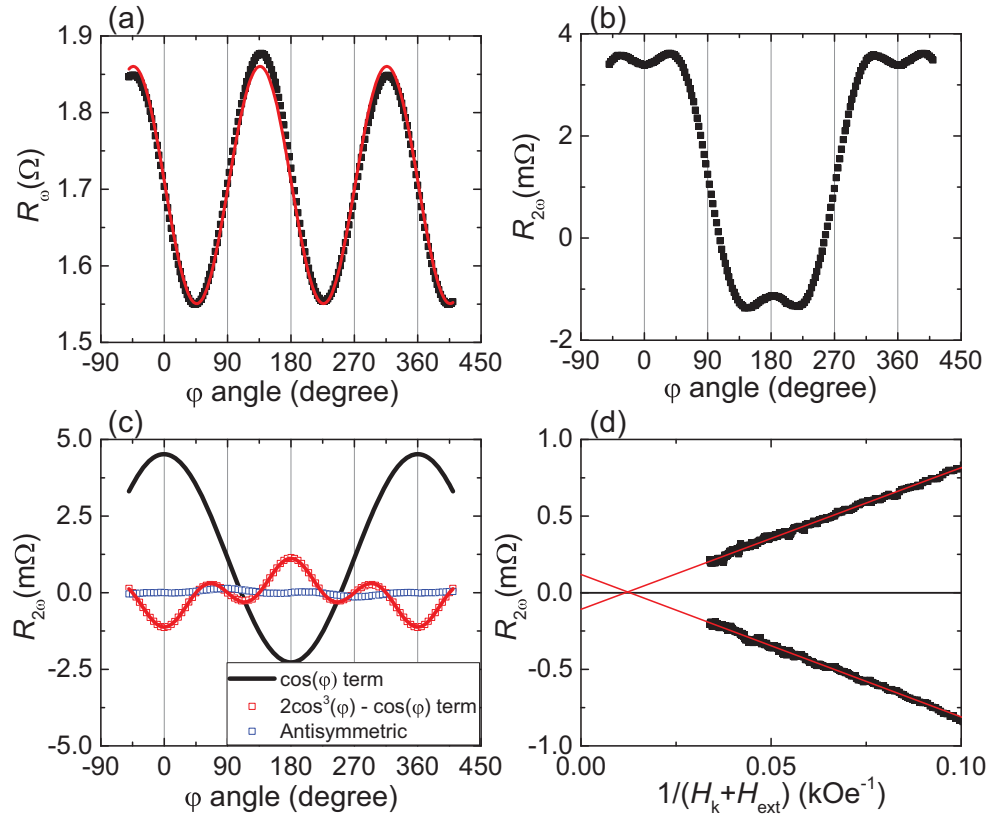

FIG. 15. (a) R_ω as a function of external field direction φ. The red line is a $\sin 2\varphi$ fit to the data. (b) $R_{2\omega}$ as a function of external field direction φ. (c) Decomposition of $R_{2\omega}$ into a "$\cos\varphi$" term and a "$2\cos^3\varphi - \cos\varphi$" term. The antisymmetric component arising from the sample misalignment is very small. (d) $R_{2\omega}$ against $\frac{1}{H_k+|H_{ext}|}$ for H_{ext} along $\varphi = 45$ and 225°. Red lines are linear fits to the data.

a combination of the Slonczewski-like torque and the inverse spin Hall voltage. The antisymmetric Lorentzian (dark yellow line in Fig. 16) is proportional to the sum of the Oersted field and the fieldlike torque. The ST-FMR spectrum of a Ta(1)/Pt(5.4)/CoFeB(3) control sample is plotted in Fig. 16(b) for comparison. Qualitatively, the fact that the symmetric Lorentzian components of the two samples are of the same sign indicates that the spin Hall angle of CoGa is of the same sign as that of Pt (positive by convention). The antisymmetric Lorentzian components of the two samples are opposite in sign, which cannot be explained by the Oersted field alone. For Ta(1)/Pt(5.4)/CoFeB(3) heterostructure, the relatively thick CoFeB layer ensures that the Oersted field contribution is the dominant source of the antisymmetric component, because the fieldlike torque scales with the inverse of the CoFeB thickness. The sign change of the antisymmetric component in the CoGa(5)/CoFeB(1) bilayer suggests that the fieldlike torque acting on the CoFeB is larger than and opposite to the Oersted field produced by the current flowing in the CoGa layer. These are all in qualitative agreement

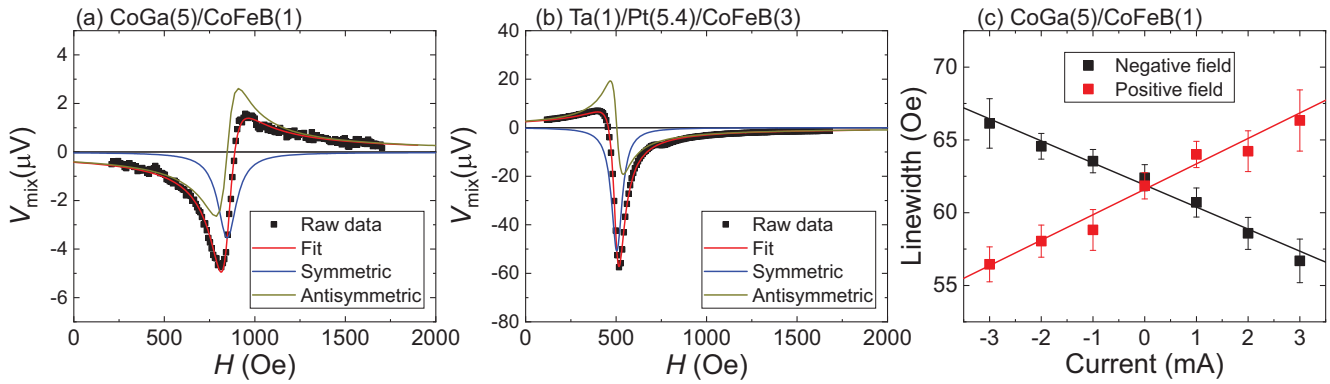

FIG. 16. Spin-torque FMR spectrum of (a) CoGa(5)/CoFeB(1) bilayer and (b) Ta(1)/ Pt(5.4)/CoFeB(3) reference stack. (c) Resonance linewidth against applied dc current demonstrating spin Hall spin current-induced modulation of Gilbert damping.

with the in-plane harmonic Hall results, shown in Figs. 3(e) and 3(f).

We evaluate the Slonczewski-like spin Hall efficiency of CoGa from the change of the resonance linewidth (hence the Gilbert damping) of the ferromagnetic CoFeB layer as a function of a dc current applied to the bilayer [Fig. 16(c)]. We find a change of the resonance linewidth per current $|\Delta'|/I_0 \sim 1.4\,\mathrm{Oe/mA}$ or in terms of the current density in CoGa, $|\Delta'|/J_0 \sim 0.85\,\mathrm{Oe}/10^6\,\mathrm{A\,cm^{-2}}$. The Slonczewski-like spin Hall efficiency is given by

$$\xi_{\mathrm{SL}} = \frac{\gamma}{2\pi f}\frac{2e}{\hbar}\frac{(H_{\mathrm{FMR}} + 2\pi M_{\mathrm{eff}})\mu_0 M_s t_{\mathrm{CoFeB}}}{|\sin\varphi|}\frac{\Delta'}{J_0}, \tag{A9}$$

where $\frac{\gamma}{2\pi} = 28\,\mathrm{GHz/T}$ is the gyromagnetic ratio, $f = 8\,\mathrm{GHz}$ is the rf frequency, $H_{\mathrm{FMR}} = 857$ Oe is the resonance field, $4\pi M_{\mathrm{eff}} = 0.86$ T is the effective demagnetizing field, $M_s = 1100\,\mathrm{emu/cm^3}$ is the saturation magnetization, and $\varphi = 45^\circ$ is the relative angle between the current and the field. We find $\xi_{\mathrm{SL}} \sim +0.073 \pm 0.015$, which is higher than but still in reasonable agreement with ξ_{SL} obtained from the harmonic Hall and the SMR measurements.

9. Estimation of the carrier mean free path

The electron mean free path l in CoGa can be estimated using an expression derived from the free electron model for a three-dimensional system [62]:

$$l = \frac{3\pi^2\hbar}{e^2 k_F^2 \rho_{\mathrm{CoGa}}}. \tag{A10}$$

ρ_{CoGa} is the longitudinal resistivity of CoGa and $k_F = \sqrt[3]{3\pi^2 n}$ is the Fermi wave vector that depends on the effective carrier density, n. We assume an effective carrier density of $\sim$1 electron per formula unit (or $n \sim 4.3 \times 10^{28}\,\mathrm{carrier/m^3}$) for CoGa, which is typical for metals. Using $\rho = 175\ \mu\Omega\,\mathrm{cm}$, we obtain $l \sim 0.59\,\mathrm{nm}$, which is very short and is of the order of two unit cells ($d \sim 0.287\,\mathrm{nm}$).

10. Details of the first-principles calculations

We consider a $B2$ structure of stoichiometric β-CoGa and use the experimentally determined lattice constant of 0.287 nm. First-principles calculations are carried out based on generalized gradient approximation [63] by using the full-potential linearized augmented plane-wave method [49], where a plane-wave cutoff of $3.9\,\mathrm{bohr^{-1}}$ has been used and a muffin-tin radius of 2.2 bohrs for Co and Ga atoms has been chosen. The intrinsic spin Hall conductivity is evaluated by means of the Kubo formula [64,65] in the static limit ($\omega = 0$), where 97 336 special k points are used to suppress numerical errors.

[1] I. M. Miron, K. Garello, G. Gaudin, P. J. Zermatten, M. V. Costache, S. Auffret, S. Bandiera, B. Rodmacq, A. Schuhl, and P. Gambardella, Nature (London) **476**, 189 (2011).

[2] L. Liu, C.-F. Pai, Y. Li, H. W. Tseng, D. C. Ralph, and R. A. Buhrman, Science **336**, 555 (2012).

[3] Y. Fan, P. Upadhyaya, X. Kou, M. Lang, S. Takei, Z. Wang, J. Tang, L. He, L.-T. Chang, M. Montazeri, G. Yu, W. Jiang, T. Nie, R. N. Schwartz, Y. Tserkovnyak, and K. L. Wang, Nat. Mater. **13**, 699 (2014).

[4] X. Qiu, K. Narayanapillai, Y. Wu, P. Deorani, D.-H. Yang, W.-S. Noh, J.-H. Park, K.-J. Lee, H.-W. Lee, and H. Yang, Nat. Nanotechnol. **10**, 333 (2015).

[5] Y.-C. Lau, D. Betto, K. Rode, J. M. D. Coey, and P. Stamenov, Nat. Nano **11**, 758 (2016).

[6] S. Fukami, C. Zhang, S. DuttaGupta, A. Kurenkov, and H. Ohno, Nat. Mater. **15**, 535 (2016).

[7] Y.-W. Oh, S.-h. Chris Baek, Y. M. Kim, H. Y. Lee, K.-D. Lee, C.-G. Yang, E.-S. Park, K.-S. Lee, K.-W. Kim, G. Go, J.-R. Jeong, B.-C. Min, H.-W. Lee, K.-J. Lee, and B.-G. Park, Nat. Nano **11**, 878 (2016).

[8] C. O. Avci, A. Quindeau, C.-F. Pai, M. Mann, L. Caretta, A. S. Tang, M. C. Onbasli, C. A. Ross, and G. S. D. Beach, Nat. Mater. **16**, 309 (2016).

[9] A. Hoffmann, IEEE Trans. Magn. **49**, 5172 (2013).

[10] C.-F. Pai, L. Liu, Y. Li, H. W. Tseng, D. C. Ralph, and R. A. Buhrman, Appl. Phys. Lett. **101**, 122404 (2012).

[11] J. Liu, T. Ohkubo, S. Mitani, K. Hono, and M. Hayashi, Appl. Phys. Lett. **107**, 232408 (2015).

[12] Y.-C. Lau and M. Hayashi, Jpn. J. Appl. Phys. **56**, 0802B5 (2017).

[13] L. Neumann, D. Meier, J. Schmalhorst, K. Rott, G. Reiss, and M. Meinert, Appl. Phys. Lett. **109**, 142405 (2016).

[14] W. Zhang, W. Han, S.-H. Yang, Y. Sun, Y. Zhang, B. Yan, and S. S. P. Parkin, Sci. Adv. **2**, e1600759 (2016).

[15] R. Ramaswamy, Y. Wang, M. Elyasi, M. Motapothula, T. Venkatesan, X. Qiu, and H. Yang, Phys. Rev. Appl. **8**, 024034 (2017).

[16] M. Obstbaum, M. Decker, A. K. Greitner, M. Haertinger, T. N. G. Meier, M. Kronseder, K. Chadova, S. Wimmer, D. Ködderitzsch, H. Ebert, and C. H. Back, Phys. Rev. Lett. **117**, 167204 (2016).

[17] J. Cramer, T. Seifert, A. Kronenberg, F. Fuhrmann, G. Jakob, M. Jourdan, T. Kampfrath, and M. Kläui, Nano Lett. **18**, 1064 (2018).

[18] A. R. Mellnik, J. S. Lee, A. Richardella, J. L. Grab, P. J. Mintun, M. H. Fischer, A. Vaezi, A. Manchon, E. A. Kim, N. Samarth, and D. C. Ralph, Nature (London) **511**, 449 (2014).

[19] Y. Niimi, Y. Kawanishi, D. H. Wei, C. Deranlot, H. X. Yang, M. Chshiev, T. Valet, A. Fert, and Y. Otani, Phys. Rev. Lett. **109**, 156602 (2012).

[20] K.-U. Demasius, T. Phung, W. Zhang, B. P. Hughes, S.-H. Yang, A. Kellock, W. Han, A. Pushp, and S. S. P. Parkin, Nat. Commun. **7**, 10644 (2016).

[21] B. F. Miao, S. Y. Huang, D. Qu, and C. L. Chien, Phys. Rev. Lett. **111**, 066602 (2013).

[22] K. Kanagawa, Y. Teki, and E. Shikoh, AIP Adv. **8**, 055910 (2018).

[23] K. Z. Suzuki, R. Ranjbar, A. Sugihara, T. Miyazaki, and S. Mizukami, Jpn. J. Appl. Phys. **55**, 010305 (2016).

[24] R. Reza, Z. S. Kazuya, S. Yuta, B. Lakhan, and M. Shigemi, Jpn. J. Appl. Phys. **55**, 120302 (2016).

[25] T. Graf, C. Felser, and S. S. P. Parkin, Prog. Solid State Chem. **39**, 1 (2011).
[26] B. Balke, G. H. Fecher, J. Winterlik, and C. Felser, Appl. Phys. Lett. **90**, 152504 (2007).
[27] S. Mizukami, F. Wu, A. Sakuma, J. Walowski, D. Watanabe, T. Kubota, X. Zhang, H. Naganuma, M. Oogane, Y. Ando, and T. Miyazaki, Phys. Rev. Lett. **106**, 117201 (2011).
[28] H. Kurt, K. Rode, M. Venkatesan, P. Stamenov, and J. M. D. Coey, Phys. Rev. B **83**, 020405(R) (2011).
[29] J. Jeong, Y. Ferrante, S. V. Faleev, M. G. Samant, C. Felser, and S. S. P. Parkin, Nat. Commun. **7**, 10276(R) (2016).
[30] D. Berner, G. Geibel, V. Gerold, and E. Wachtel, J. Phys. Chem. Solids **36**, 221 (1975).
[31] W. Zhang, W. Han, X. Jiang, S.-H. Yang, and S. S. P. Parkin, Nat. Phys. **11**, 496 (2015).
[32] H. Nakayama, M. Althammer, Y. T. Chen, K. Uchida, Y. Kajiwara, D. Kikuchi, T. Ohtani, S. Geprägs, M. Opel, S. Takahashi, R. Gross, G. E. W. Bauer, S. T. B. Goennenwein, and E. Saitoh, Phys. Rev. Lett. **110**, 206601 (2013).
[33] M. Althammer, S. Meyer, H. Nakayama, M. Schreier, S. Altmannshofer, M. Weiler, H. Huebl, S. Geprägs, M. Opel, R. Gross, D. Meier, C. Klewe, T. Kuschel, J.-M. Schmalhorst, G. Reiss, L. Shen, A. Gupta, Y.-T. Chen, G. E. W. Bauer, E. Saitoh, and S. T. B. Goennenwein, Phys. Rev. B **87**, 224401 (2013).
[34] J. Kim, P. Sheng, S. Takahashi, S. Mitani, and M. Hayashi, Phys. Rev. Lett. **116**, 097201 (2016).
[35] Y.-T. Chen, S. Takahashi, H. Nakayama, M. Althammer, S. T. B. Goennenwein, E. Saitoh, and G. E. W. Bauer, Phys. Rev. B **87**, 144411 (2013).
[36] J. Kim, J. Sinha, M. Hayashi, M. Yamanouchi, S. Fukami, T. Suzuki, S. Mitani, and H. Ohno, Nat. Mater. **12**, 240 (2013).
[37] K. Garello, I. M. Miron, C. O. Avci, F. Freimuth, Y. Mokrousov, S. Blugel, S. Auffret, O. Boulle, G. Gaudin, and P. Gambardella, Nat. Nano **8**, 587 (2013).
[38] C. O. Avci, K. Garello, M. Gabureac, A. Ghosh, A. Fuhrer, S. F. Alvarado, and P. Gambardella, Phys. Rev. B **90**, 224427 (2014).
[39] M. Hayashi, J. Kim, M. Yamanouchi, and H. Ohno, Phys. Rev. B **89**, 144425 (2014).
[40] L. Liu, T. Moriyama, D. C. Ralph, and R. A. Buhrman, Phys. Rev. Lett. **106**, 036601 (2011).
[41] A. Manchon, H. C. Koo, J. Nitta, S. M. Frolov, and R. A. Duine, Nat. Mater. **14**, 871 (2015).
[42] M. D. Stiles and A. Zangwill, Phys. Rev. B **66**, 014407 (2002).
[43] P. M. Haney, H.-W. Lee, K.-J. Lee, A. Manchon, and M. D. Stiles, Phys. Rev. B **88**, 214417 (2013).
[44] J. Kim, J. Sinha, S. Mitani, M. Hayashi, S. Takahashi, S. Maekawa, M. Yamanouchi, and H. Ohno, Phys. Rev. B **89**, 174424 (2014).
[45] Y. Ou, C.-F. Pai, S. Shi, D. C. Ralph, and R. A. Buhrman, Phys. Rev. B **94**, 140414 (2016).
[46] Hamed Ben Mohamed Saidaoui and A. Manchon, Phys. Rev. Lett. **117**, 036601 (2016).
[47] V. P. Amin and M. D. Stiles, Phys. Rev. B **94**, 104419 (2016).
[48] V. P. Amin and M. D. Stiles, Phys. Rev. B **94**, 104420 (2016).
[49] K. Nakamura, T. Ito, A. J. Freeman, L. Zhong, and J. Fernandez-de-Castro, Phys. Rev. B **67**, 014420 (2003).
[50] G. L. Whittle, G. C. Fletcher, P. E. Clark, and R. Cywinski, J. Phys. F **12**, 303 (1982).
[51] A.-M. Pradipto, T. Akiyama, T. Ito, and K. Nakamura, Phys. Rev. B **97**, 024401 (2018).
[52] S. Nakatsuji, N. Kiyohara, and T. Higo, Nature (London) **527**, 212 (2015).
[53] A. K. Nayak, J. E. Fischer, Y. Sun, B. Yan, J. Karel, A. C. Komarek, C. Shekhar, N. Kumar, W. Schnelle, J. Kübler, C. Felser, and S. S. P. Parkin, Sci. Adv. **2**, e1501870 (2016).
[54] Y. Zhang, Y. Sun, H. Yang, J. Zelezny, S. P. P. Parkin, C. Felser, and B. H. Yan, Phys. Rev. B **95**, 075128 (2017).
[55] K. Rode, N. Baadji, D. Betto, Y.-C. Lau, H. Kurt, M. Venkatesan, P. Stamenov, S. Sanvito, J. M. D. Coey, E. Fonda, E. Otero, F. Choueikani, P. Ohresser, F. Porcher, and G. André, Phys. Rev. B **87**, 184429 (2013).
[56] H. Kurt, K. Rode, P. Stamenov, M. Venkatesan, Y. C. Lau, E. Fonda, and J. M. D. Coey, Phys. Rev. Lett. **112**, 027201 (2014).
[57] D. Betto, Y.-C. Lau, K. Borisov, K. Kummer, N. B. Brookes, P. Stamenov, J. M. D. Coey, and K. Rode, Phys. Rev. B **96**, 024408 (2017).
[58] A. K. Nayak, M. Nicklas, S. Chadov, P. Khuntia, C. Shekhar, A. Kalache, M. Baenitz, Y. Skourski, V. K. Guduru, A. Puri, U. Zeitler, J. M. D. Coey, and C. Felser, Nat. Mater. **14**, 679 (2015).
[59] H. Lee, H. Sukegawa, J. Liu, S. Mitani, and K. Hono, Appl. Phys. Lett. **109**, 152402 (2016).
[60] S. Vélez, V. N. Golovach, A. Bedoya-Pinto, M. Isasa, E. Sagasta, M. Abadia, C. Rogero, L. E. Hueso, F. S. Bergeret, and F. Casanova, Phys. Rev. Lett. **116**, 016603 (2016).
[61] Y.-C. Lau, P. Sheng, S. Mitani, D. Chiba, and M. Hayashi, Appl. Phys. Lett. **110**, 022405 (2017).
[62] O. Gunnarsson, M. Calandra, and J. E. Han, Rev. Mod. Phys. **75**, 1085 (2003).
[63] J. P. Perdew, K. Burke, and M. Ernzerhof, Phys. Rev. Lett. **77**, 3865 (1996).
[64] P. M. Oppeneer, T. Maurer, J. Sticht, and J. Kübler, Phys. Rev. B **45**, 10924 (1992).
[65] G. Y. Guo, Y. Yao, and Q. Niu, Phys. Rev. Lett. **94**, 226601 (2005).